

1 Flood Characteristic and Fluid Rock
2 Interactions of a Supercritical CO₂, Brine,
3 Rock System: South West Hub, Western
4 Australia

5

6

7 Dr Ali Saeedi: Department of Petroleum Engineering, Curtin University, Western Australia

8 Dr Claudio Delle Piane: CSIRO Energy, Western Australia

9 Dr Lionel Esteban: CSIRO Energy, Western Australia

10 Dr Quan Xie: Department of Petroleum Engineering, Curtin University, Western Australia

11 **Contact details of the corresponding author**

12 **Name:** Ali Saeedi

13 **Address:** 26 Dick Perry Avenue, Kensington, WA 6151, Australia

14 **Tel:** +61 8 9266 4988

15 **Email:** Ali.Saeedi@Curtin.edu.au

16 **1 Abstract**

17 Chemical and/or physical interactions between the storage rock and injected and in-situ created solutes
18 are expected to occur during many underground CO₂ storage projects. The intensity of the reactions,
19 however, depends on the abundance of susceptible minerals (e.g. carbonates, clays) in the pore space
20 of the host rock. Such interactions may impact on the multiphase flow characteristics of the underground
21 fluids-rock system over short as well as long time frames.

22 In this research the in-situ multiphase flow characteristics of four sandstone samples have been
23 investigated using a set of laboratory measurements. The samples tested were taken from the Wonnerup
24 Member of the Triassic Lesueur Sandstone which is under consideration as a storage formation in the
25 South-West Hub CO₂ geo-sequestration site in Western Australia.

26 All the samples tested show favourable characteristics in terms of storage capacity in the form of
27 residual capillary trapping with residual CO₂ saturation varying between 23% and 43%. They
28 underwent a degree of alteration to their petrophysical characteristics which was most significantly
29 pronounced in the case of their absolute gas permeability which showed drops of 25% to 60% in the
30 post-flood samples. Formation damage by fines migration is proposed as a mechanism for the observed
31 reduction in permeability. The fines are believed to have originated from the kaolinite particles present
32 in the pore space of the samples.

33 **2 Introduction**

34 Geologic carbon sequestration, i.e. the storage of CO₂ into buried geologic reservoir formations, is being
35 developed worldwide and considered as a large scale greenhouse gas mitigation technology (IPCC,
36 2005). In Western Australia, the Perth Basin is being investigated as a potential site for CO₂ injection
37 due to the presence of large and relatively deeply buried saline aquifer in the proximity of industrial
38 emitters.

39 The successful operation and management of industrial scale projects require, among others, accurate
40 characterization of the injectivity of CO₂ into the reservoir rocks and of their storage potential in
41 advance during the planning stage of the projects. Injectivity is affected by the rock properties, the
42 nature of the fluids and the in-situ conditions at depth and a proper assessment of these variables is
43 therefore critical for the planning of any geo-sequestration project.

44 The South-West CO₂ Geo-sequestration Hub project (the South-West Hub) is one of the Australian
45 Flagship Carbon Capture and Storage Projects, a government funded initiative in partnership with major
46 local industrial CO₂ emitters. The project aims to explore the potential of storing commercial quantities
47 of CO₂ in a deep saline aquifer as part of a precompetitive data gathering effort. As part of the early
48 stages of the South-West Hub project, a stratigraphic well (Harvey-1) was drilled in 2012 by the
49 Geological Survey of Western Australia (Millar and Reeve, 2014) to confirm the stratigraphy of the
50 area and recover core material to be tested in the laboratory (Figure 1).

51 The potential storage target in the South-West Hub area consists of the Triassic Lesueur Sandstone
52 subdivided into the upper Yalgorup and the lower Wonnerup Members (Figure 1). Due to the lack of
53 outcrops, the knowledge of the potential reservoir rocks properties is limited to the sparse available
54 material sampled from old exploration wells (see Delle Piane et al., 2013a; Delle Piane et al., 2013b;
55 Dillinger and Esteban, 2014 and Timms et al., 2015), the new core material extracted from the Harvey-
56 1 well is therefore invaluable for the progress of the South-West Hub project.

57 Relative permeability of the underground rock-fluids system influences the injectivity and subsurface
58 movement of CO₂ and reservoir simulations are usually used to predict the CO₂ injection capacity and
59 plume migration at a full reservoir scale. The key parameters used to determine the multiphase
60 (formation brine and CO₂) fluids mobility and distribution in the subsurface are relative permeability in
61 addition to porosity and permeability of the host rock (e.g. Doughty and Pruess, 2004; Kopp et al. 2009).
62 Whereas porosity and permeability can be readily obtained from inversion of wireline log parameters
63 or routine laboratory measurements, relative permeability is inherently more difficult to derive and
64 requires special experimental protocols and equipment (e.g. Muller, 2011).

65 Two principal approaches are used to obtain a relative permeability data from laboratory measurements:
66 i) steady state (SS) and ii) unsteady state (USS) core flooding experiments. A SS experiment consists
67 of a number of steps with every step consisting of simultaneous injection of the two fluids at a fixed
68 ratio through a porous rock sample. For every ratio, the constant flow rate injection continues until
69 saturation and differential pressure along the sample stabilise and the produced ratio equals the injected
70 ratio (Bear, 1988; Dullien, 1992). Usually, SS experiments are very time consuming and require a long
71 time for flow stabilization.

72 During USS experiments, there is no simultaneous injection of the two fluid phases and one fluid phase
73 is displaced from the saturated core sample by injecting another fluid. Contrary to the steady-state
74 techniques, there is only one injection step involved in an USS experiment, making this type of
75 experiment less time consuming (Dullien, 1992; Bear, 1988).

76 Laboratory based studies aimed at measuring the residually trapped amount of CO₂ in brine saturated
77 sandstones and supercritical conditions include the works of Bennion and Bachu (2005), Suekane et al.
78 (2008), Pentland et al. (2011), Saeedi et al. (2011), Shi et al. (2011), Lu et al. (2012), Saeedi (2012),
79 Akbarabadi and Piri (2013), Ruprecht et al. (2014), Zuo and Benson (2014), Li et al. (2015). The data
80 available in the literature globally indicates that the saturation of residually trapped CO₂ is likely to be
81 at least 10% of the pore volume and many rocks are capable of residual trapping at saturations between
82 30 and 40% of the pore volume; this is predominantly controlled by the pore scale structure of a given
83 rock type and less by the external conditions acting on the reservoirs (Krevor et al., 2015). It is worth

84 noting that the above figures are stated based on the statistical analysis of results from the core-scale
85 experiments conducted in the laboratory. At the much larger field-scale, other factors such as large scale
86 formation heterogeneities in all three directions and slower frontal displacement velocities are expected
87 to impact on the capacity of the rocks to residually trap CO₂. The impact of such factors needs to be
88 taken into account when upscaling the core-scale laboratory results to the full field-scale using
89 numerical simulation modelling techniques.

90 The main objective of this study was to investigate the multiphase flow characteristics of the
91 supercritical CO₂ (scCO₂)-brine-rock system pertinent to the South-West Hub project. Four core-
92 flooding experiments were conducted under reservoir conditions on four representative plugs sampled
93 from the core material recovered from the Harvey-1 well. All four core-plugs belonged to the Wonnerup
94 Member of the Lesueur Formation and were chosen as characteristic of the lithofacies type likely to
95 represent the injection target (for details on lithofacies characteristics see Delle Piane et al., 2013b;
96 Olierook et al., 2014 and Timms et al., 2015). The core-flooding experiments were performed using a
97 conventional USS procedure (as briefly described earlier) with the main focus of obtaining the relative
98 permeabilities and residual saturations.

99 In addition to the main core-flooding experiments, a number of auxiliary petrophysical measurements
100 were also carried out on the samples before and after the floods (e.g. helium porosity-permeability and
101 pore body size distribution converted from relaxation time T₂ spectra by low field nuclear magnetic
102 resonance (NMR) measurements). The purpose of these complementary measurements was to
103 investigate any potential alterations of the petrophysical properties of the samples induced by the
104 flooding procedure.

105 **3 Experimental Measurements**

106 **3.1 Material and initial sample characterisation**

107 Four horizontal (i.e. cored perpendicular to the whole-core axis) core-plugs were selected from the
108 cored sections of Harvey-1 at depths considered relevant to the injection operations in the proposed

109 South-West Hub. The samples belonged to the lithofacies type of the Wonnerup Member of the Triassic
110 Lesueur Sandstone described as interbedded coarse to gravelly cross-bedded sandstones, deposited in
111 high-energy river channel fill and barforms (facies Ai and Aii as described by Delle Piane et al., 2013a;
112 Olierook et al., 2014, Timms et al., 2015).

113 The core plugs were drilled dry from the whole-cores recovered from well Harvey-1. Upon recovery,
114 the whole-cores were depressurised at the well site and laid into standard core trays before being
115 transferred to the core storage facility where core plugs were drilled dry using a 3.81 cm (1.5") coring
116 bit. Upon cutting and trimming, the core plugs were subjected to a core cleaning process using warm
117 toluene and methanol in a temperature controlled Dean-Stark apparatus to remove any possible
118 contaminants (e.g. salts, possible hydrocarbons) from the samples before they undergo any of the
119 subsequent experimental measurements. Subsequently the samples were dried in an oven for 48 hours
120 under a temperature of 105°C. The post-flood samples were dried and their salt residues were cleaned
121 using an approach similar to the above but only in the last stage when gas porosity-permeability
122 measurements were performed. From the initial saturation stage to some of the analysis performed on
123 the post-flood samples, the plugs never underwent any dehydration to avoid salt precipitation from the
124 brine. Therefore, NMR, brine permeability and core flooding before and after experiments were
125 acquired with the same hydration status.

126 A general characterization was performed on three of the four samples (206647, 206660 and 206669)
127 by means of X-ray diffraction (XRD), mercury injection, Helium porosity and permeability and nuclear
128 magnetic resonance (NMR), while sample 206655 underwent helium porosity and permeability
129 measurements only and 206669 underwent NMR on pre-flooding experiments only.

130 Porosity and gas permeability were measured using an automated helium porosimeter-permeameter (AP
131 608 from Coretest Systems Inc.) at effective stresses of 1.72, 5.2 and 32.7 MPa; at each level of pressure
132 the measurements were repeated three times to assess their reproducibility. Brine permeability of each
133 sample was also measured at the beginning of the core-flooding experiments under in-situ reservoir
134 conditions using a synthetic formation brine with salinity of 30,000 ppm NaCl. This formation water

135 salinity was chosen based on the interpretation results of the resistivity logs run in well Harvey-1 only
136 as no representative formation water samples could be collected from the well.

137 X-ray tomographic (XCT) images of three of the four samples were acquired using a Toshiba Asteion
138 medical scanner to evaluate the internal structures and the integrity of the plugs. The processed XCT
139 images were oriented at the maximum bedding angle within each plug sample and show well developed
140 sedimentary beds in the three plugs; these are either parallel or slightly inclined to the plugs axes (Figure
141 2a).

142 Mercury Injection Capillary Pressure curves (MICP) were acquired on cubic offcuts (with side of
143 approximately 0.7 cm) of three of the core plugs to analyse their pore size distribution. The offcuts were
144 cut from the core plugs after undergoing the earlier outlined cleaning procedure. The offcuts were
145 placed in a Micromeritics Autopore IV porosimeter under vacuum and injected with mercury at about
146 120 increasing capillary pressure steps to a maximum pressure of 413 MPa (equivalent to 2-3 nm pore
147 throat size).

148 Finally, the sample characterization was completed by low field NMR measurements conducted using
149 a Maran 2 MHz Ultra-spectrometer (Oxford Instruments Ltd) on three core plugs (206647, 206660 and
150 206669) before and after flooding experiments to evaluate possible changes in porosity and pore size
151 distribution induced by the flooding tests. For NMR measurements before the flooding experiments,
152 the samples were brine saturated under vacuum for 48 hours and then analysed. After the flooding
153 experiments, the brine saturated samples were reanalysed using the protocol previously applied on the
154 same samples. Note that samples 206669 and 206655 could not be properly preserved after core
155 flooding and the post-flood NMR was not recorded for these samples. The difference in mass between
156 the dry and brine-saturated core-plugs was used to calculate their water-filled porosity (Water
157 Imbibition Porosity - WIP). Also, assessment of full saturation was made by comparing the WIP to the
158 helium porosity. Once saturated, the samples were tested in the NMR spectrometer using a Carr–
159 Purcell–Meiboom–Gill (CPMG) pulse sequence following the protocol described in the literature (e.g.
160 Dillinger and Esteban, 2014). This spin-echo method records the pore size distribution, similar to

161 mercury porosimetry, using the transverse magnetic relaxation time (T_2). In an NMR test the
162 magnetization and transverse relaxation time (T_2) of hydrogen nuclei contained in the pore fluid is
163 measured. Different pore sizes in fluid saturated rocks will produce characteristic T_2 distributions as the
164 amplitude of transverse magnetization is proportional to the number of hydrogen nuclei (Dunn et al.,
165 2002). As a consequence, the observed T_2 distribution of a saturated core sample can be converted into
166 pore size distribution of the rock using literature data transform from sandstones (Jorand et al., 2011;
167 Kleinberg et al., 2003a; Kleinberg et al., 2003b). The Maran 2 MHz and the experimental protocol
168 ensure a resolution of pore body size about 0.1 μm assuming that no or little amount of paramagnetic
169 and ferromagnetic minerals, such as magnetite or metalloids, perturbate the T_2 relaxation (Nicot et al.,
170 2006).

171 **3.2 Core-flood Setup**

172 Table 1 lists the pressure and temperature values used during the experiments; for each sample, the
173 pressure, temperature and salinity values correspond to those at the depth from which the sample was
174 recovered. The fluids used during the various stages of this experimental work consisted of deaerated
175 dead formation brine (i.e. formation brine with no gas content), CO_2 -saturated brine and water vapour-
176 saturated sc CO_2 . The CO_2 gas used was of at least 99.9 mol % purity. Formation brine and CO_2 were
177 mutually saturated with each other in a stirred Parr reactor under in-situ conditions. The formation brine
178 was prepared in the lab using distilled water and appropriate amounts of analytical grade sodium
179 chloride (NaCl) supplied by Sigma-Aldrich.

180 The experiments were carried out using a high pressure-high temperature, three-phase steady-state core-
181 flooding apparatus. A schematic of the core-flooding rig is presented in Figure 3. Comprehensive details
182 on the specifications of the core-flooding apparatus can be found elsewhere (Saeedi, 2012; Saeedi et
183 al., 2011).

184 **3.3 Core-flood Procedure**

185 During the core-flooding experiments a specially designed multi-layered combination sleeve was used.
186 This combination sleeve was utilised to prevent the diffusion of CO_2 which normally occurs through

187 most conventional flexible rubber sleeves. A full description of various components of the sleeve is
188 presented elsewhere (Saeedi et al., 2011). In order to eliminate the effect of gravity segregation (i.e.
189 underrun or override of the injected fluids) the core-holder containing the sample was placed vertically
190 so the injection would be performed from the base to the top. In order to apply overburden pressure to
191 the sample, after loading the wrapped sample into the core-holder, using a hand pump, the overburden
192 fluid was pumped slowly into the annular space of the core holder.

193 Below is an outline of the steps involved in carrying out the conventional USS core-flooding
194 experiments. This procedure has been designed based on the standard procedures and protocols
195 available in the literature (Bennion and Bachu, 2005; Izgec et al., 2008; Perrin and Benson, 2010; Saeedi
196 et al., 2011).

- 197 1. After loading a sample into the core-holder and gradually increasing the overburden pressure to the
198 reservoir net effective stress, low pressure CO₂ gas was passed through the sample for at least 20
199 minutes to displace and replace the air present in the sample's pore space. Compared to air, the
200 CO₂, due to its small sized molecules and higher diffusivity (Baker and Low, 2014), could be
201 evacuated from the sample more effectively when required. Furthermore, any remaining CO₂ after
202 evacuation would readily dissolve in the saturating dead brine and removed from the sample during
203 the later in-situ saturation and initial brine permeability measurement process.
- 204 2. After flushing the sample with CO₂, all the flow-lines and the sample inside the core-holder were
205 vacuumed using a vacuum pump for at least 24 hours. Then the back pressure was brought to full
206 in-situ reservoir pressure, and the air bath temperature was raised to the reservoir temperature. Then
207 the core sample was saturated using dead formation brine while the confining pressure was
208 increased and then maintained equal to its in-situ reservoir value. The sample was left under
209 reservoir conditions in contact with brine for another 48 hours to become completely saturated with
210 dead brine and to establish adsorption equilibrium. The full saturation was confirmed by the
211 constant pressure reading from the injection pump, which maintained the pore pressure of the core
212 sample during the above 48 hours. For some of the experimental work where the sample could be
213 accessed during the saturation with minimum effort (e.g. core saturation for the NMR tests), the

214 volume of injected brine was also tracked from mass intake assuming a brine density of 1.03 g/cc
215 and compared to pore volume from gas porosity measurements to ensure complete saturation (>
216 98% in all the tested plugs).

217 3. In the next step, the CO₂-saturated brine was injected into the core sample at constant flow-rate to
218 displace the dead formation brine. The CO₂-saturated brine injection continued until steady-state
219 conditions were achieved (i.e. constant and steady differential pressure across the sample and
220 production flow-rate was equal to injection flow-rate).

221 4. Then, the injection of the vapour-saturated scCO₂ began at constant flow-rate (primary drainage
222 flood). The displacement continued until steady-state conditions were reached. At the conclusion
223 of this drainage process there was a so called “bump flow” (i.e. a short period of high injection
224 flow-rate) performed to examine and quantify the existence of any capillary end-effect (Rapoport
225 and Leas, 1953; Heaviside and Black, 1983; Grigg and Svec, 2006).

226 5. After the conclusion of the primary drainage, the core-sample was subjected to the primary
227 imbibition flood. CO₂-saturated brine was injected into the sample at constant flow-rate. The brine
228 injection continued until the steady-state conditions were achieved.

229 6. In the next step, for two of the experiments, the sample underwent another cycle of drainage-
230 imbibition floods (secondary drainage and imbibition). For this purpose, steps number 5 and 6 were
231 repeated again.

232 7. At the conclusion of the experiment, the core-holder was depressurised and the core sample was
233 removed.

234 It is worth noting that during the procedure outlined above all the injected fluids passed through a 0.5
235 micron sintered stainless steel line filter before entering the core samples. This was to prevent any
236 external fines being pushed into the pore space of the samples and potentially block and/or bridge the
237 samples' pore channels.

238 **4 Results**

239 **4.1 General characterization**

240 Quantitative mineralogy by X-Ray Diffraction (XRD) indicates quartz and K-feldspar as the main
241 constituents of these sandstones, with accessory kaolinite (up to 7% in sample 206660) (Table 2).
242 Furthermore, sample 206660 contained 4% of ankerite, a calcium, iron, magnesium, manganese
243 carbonate.

244 Table 2 summarizes the petrophysical properties of the pre-flood core-plugs, i.e. mercury porosity,
245 helium porosities and permeabilities measured at the lowest effective stress (1.72 MPa) and brine
246 permeability as well as mineralogy as measured by XRD. All the core-plugs displayed comparable
247 values of porosity but a wider range of helium permeability (from 25 to 532 mD) and brine permeability
248 (from 4.65 to 238 mD); also there is a good agreement between porosity measured by mercury injection
249 on small offcuts (Figure 2c) and the values retrieved via He-porosimetry on the full core plugs. On the
250 other hand, there is a significant difference between the values of He and water permeability. This is
251 due the well-known Klinkenberg effect which is well described in the literature (Tiab and Donaldson,
252 2004).

253 Following the definition outlined by Sing et al. (1984), pore sizes can be classified as follows:

- 254 • Micropores: with widths smaller than 2 nm.
- 255 • Mesopores: with widths between 2 and 50 nm.
- 256 • Macropores: with widths larger than 50 nm.

257 MICP results show similar pattern for the three analysed samples (Figure 2b) with a narrow population
258 of mesopores (cumulatively 2.5 to 3.5 % of the pore volume) while the rest of the pore sizes fall in the
259 macropores range (> 50 nm); micropores could not be detected in the analysed samples. Samples
260 206647 and 206669 have a dominant pore population with throat diameter of ≈ 40 μm , while sample
261 206660 has a broad distribution of pores and the largest detected throat size of ≈ 30 μm which can
262 explain its lower permeability with respect to the other samples.

263 **4.2 Core flood tests**

264 As indicated earlier, samples 206647 and 206669 underwent successive primary and secondary
265 drainage and imbibition floods but samples 206655 and 206660 were tested for primary drainage and
266 imbibition floods only. For all four samples, the end-point residual saturations obtained at the end of
267 the drainage and imbibition floods are presented in Table 3 along with the corresponding end-point
268 relative permeabilities for the displacing fluids.

269 Figure 4 shows the brine productions versus pore volumes of scCO₂ injected through the samples for
270 the primary drainage floods conducted on all four samples. As may be expected, there is considerable
271 volume of brine produced after scCO₂ breakthrough in the case of sample 206647. This may be
272 attributed mainly to the high permeability of this sample leading to a more non-uniform or dispersed
273 displacement (Saeedi et al., 2011; Saeedi, 2012) compared to other samples whose post breakthrough
274 brine production profiles are comparable. The relative permeability curves corresponding to the above
275 mentioned brine production profiles for three of the samples are also shown in Figure 5. While the end-
276 point scCO₂ relative permeabilities for all samples are comparable, the curvature of the plots changes
277 according to the samples permeabilities (i.e. the higher the permeability the higher the curvature). It is
278 worth noting that the relative permeability data provided here were calculated using a numerical history
279 matching technique (Archer and Wong, 1973; Sigmund and McCaffery, 1979; Bennion and Bachu,
280 2005). Sendra software from PRORES AS, which is based upon a two-phase, 1D black-oil simulation
281 model together with an automated history matching routine, was used to reconcile time and spatially
282 dependent experimental data and generate the relative permeabilities. This technique has three primary
283 advantages over other relative permeability derivation techniques such as the JBN (Johnson, Bossler,
284 and Naumann): 1. The relative permeability data can be derived directly for the full range of mobile
285 scCO₂ and brine saturations and there is no need for extrapolation of this data as commonly done in
286 other techniques such as the JBN, 2. Unlike other techniques such as the JBN where the effect of
287 capillary pressure is ignored, the technique used here takes into account the effect of capillary pressure
288 data. If such data is not available, a suitable model can be chosen to be used during the modelling and
289 history matching procedure, 3. The output relative permeability data are automatically matched using

290 one of the most commonly used relative permeability correlations (e.g. Corey, Sigmund and McCaffery,
 291 LET, etc.). This facilitates the integration of the derived relative permeability data into a full field
 292 numerical simulation model.

293 After performing the history matching routine for relative permeability calculation, the model proposed
 294 by Sigmund and McCaffery (1979) (Equations 1 to 3) was found to closely reproduce the measured
 295 data. This model was initially developed for interpretation of USS relative permeability measurements
 296 in heterogeneous cores where viscous–capillary effects are expected to be large and gravity effects are
 297 expected to be negligible. Thus, the Sigmund and McCaffery model is an ideal tool for interpreting the
 298 core–flood experiments performed here. Table 4 presents the values of the model parameters which
 299 resulted in the best match of the lab measured data by the Sigmund and McCaffery (1979) model.

$$k_{rw} = k_{rw}^0 \frac{(S_w^*)^{N_w} + AS_w^*}{1 + A} \quad \text{Eq. 1}$$

$$k_{rg} = k_{rg}^0 \frac{(1 - S_w^*)^{N_g} + B(1 - S_w^*)}{1 + B} \quad \text{Eq. 2}$$

$$S_w^* = \frac{S_w - S_{wi}}{1 - S_{wi} - S_{gi}} \quad \text{Eq. 3}$$

300 where: k_{rw} and k_{rg} are the water and gas relative permeabilities at any saturation level.

301 k_{rw}^0 and k_{rg}^0 are the end-point (maximum) water and gas relative permeabilities.

302 S_w^* is the normalised water saturation as determined by Eq. 3.

303 S_{wi} and S_{gi} are the fixed residual water and gas saturations, respectively.

304 S_w is the variable water saturation measured during an USS experiment.

305 N_w , N_g , A and B are empirical constants used for the calculation of the relative permeabilities.

306 With regards to the experiments conducted in this work, in the above equations, subscript *w* would refer
307 to the brine and subscript *g* would refer to scCO₂.

308 In an attempt to compare the results of the modelling work performed using Sendra with the output of
309 another widely used numerical simulation software package, for Sample 206655, Eclipse simulation
310 software (Schlumberger Inc.) was used to perform a core scale numerical simulation. For this task, after
311 constructing a core scale grid model in Eclipse and populating the model with basic rock and fluid
312 properties, the relative permeability data derived from Sendra were used as input data to simulate and
313 generate the brine production and differential pressure profiles. Then a comparison was made between
314 the experimental pressure and brine production data, which were fed into Sendra in the first place, and
315 their simulated counterparts. As can be seen from figures 6 and 7, there is a very close agreement
316 between the two sets of data. The rock and fluid properties used in the core scale model created using
317 Eclipse are provided in Table 5.

318 Helium porosity and permeability as well as NMR porosity (and computed permeability) measured
319 before and after core flooding experiments are summarized in Table 6. While porosity, measured by
320 Helium and NMR, does not seem to be affected by the flooding procedure, permeability values
321 significantly differ when measured on the same sample before and after flooding. Indeed, for sample
322 206647, the helium permeability measurement conducted on the post-flood dry sample showed a
323 reduction of almost 25% compared to that of the pre-flood conditions. Samples 206655, 206660 and
324 206669 also showed permeability reductions of 60%, 51% and 44%, respectively. Using a classical T₂
325 surface relaxivity in sandstones from literature of about 20 μm/s (Marschall et al, 1995; Liu et al., 2014),
326 the relaxation time T₂ distribution can be transformed into pore diameter distribution (Figure 8)
327 assuming sphere-model for the pore network topology (Dunn et al., 2002; Sorland et al., 2007) as:

$$\frac{1}{T_2} = \rho \frac{S}{V} \cong \rho \frac{3}{r} \quad \text{Eq. 4}$$

328 where *S* and *V* represent the surface and volume of the pore network, *ρ* is the surface relaxivity and *r* is
329 the pore radius. Therefore, the equation 4 can be re-arranged as:

$$d_{NMR} = 6T_2\rho_{T_2} \quad \text{Eq. 5}$$

330 where d_{NMR} is the pore body diameter (in μm) and ρ_{T_2} is the surface relaxivity of about 20 $\mu\text{m/s}$ for
331 sandstones.

332 The converted NMR pore size distribution from the T_2 spectra using the equation 5 collected on
333 samples 206647 and 206660 are shown in Figure 8 before and after flooding. The NMR pore size
334 distribution and MICP pore throat size distribution (Figure 2a) give the same range of pore size on the
335 pre-flooded samples with most of the pore size (or pore throat size) between 10 and 100 μm for 206647
336 and between 1 and 10 μm in 206660. The integrated NMR T_2 spectra curves give porosity values of
337 about 14 and 15 % for samples 206647 and 206660, respectively, very similar to MICP and helium
338 porosity data; remarkably the distributions collected in the samples after flooding show significant
339 difference with respect to those collected before flooding. Specifically, it is observed that in both
340 samples the curves are shifted towards shorter T_2 relaxation times; assuming a similar surface relaxivity
341 (i.e. similar mineralogy and surface texture of the mineral in the pre- and post-flood samples), changes
342 in the NMR T_2 relaxation time distribution in post-flood samples reflect alteration to the pore size
343 distribution in the samples. In both samples, the larger pores observed at the right end of the spectrum
344 seem to have disappeared after the flooding tests ($> 80 \mu\text{m}$ in 206647 and $> 4 \mu\text{m}$ in 206660) in favour
345 of a higher relative proportion of medium size pores occurring at $T_2 = 2 \times 10^5$ and 10^4 ms for sample
346 206647 and 206660, respectively; which correspond after conversion into pore diameter at 30 μm in
347 206647 and 1.5 μm in 206660 (Figure 8).

348 **5 Discussion**

349 **5.1 Residual trapping potential of the Lesueur Sandstone**

350 The experimental results presented above provide the first assessment of multi-phase fluid flow
351 behaviour in the potential reservoir of the South West Hub project, onshore Western Australia. As such,
352 the relative permeability functions and measured end-point residual saturations can be used to populate
353 large scale reservoir models to predict CO_2 injectivity and plume mobility over time. It is worth noting

354 that the flood characteristics of the fluid-rock system (e.g. relative permeabilities) change continuously
355 during the CO₂-brine flooding performed in the laboratory. Such changes are induced by the fluid-rock
356 interactions which occur during such experiments. According to the Darcy's Law, with the occurrence
357 of such reactions, the concept of relative permeability (which is based on and calculated using the
358 Darcy's Law) may lose its meaning. Therefore, the application of the data reported in this study and
359 perhaps other similar studies, is subject to the inherent uncertainties introduced due to the above
360 mentioned reactions and transient effects.

361 In discussing the results of the core flooding tests, the maximum CO₂ saturation achieved during the
362 drainage and the trapped saturation after the imbibition floods are referred to as S_{max} and S_t , respectively,
363 following the nomenclature commonly used in the literature (e.g. Burnside and Naylor, 2014) and use
364 the ratio of S_t to S_{max} (i.e. R) to assess the fraction of CO₂ immobilised in the pore space of a sample.
365 These parameters are useful to quantify the residual trapping potential of the Lesueur Sandstone and
366 help predict its impact on the CO₂ storage security at the reservoir scale.

367 Figure 9 illustrate the relationship between S_{max} and S_t obtained on the four samples of Lesueur
368 Sandstone tested in this study in comparison with experimental data obtained on sandstone samples
369 from different studies available in the open literature (Bennion and Bachu, 2008; ; Mackay et al., 2010;
370 Pentland et al., 2011a, b; Shell, 2011; Shi et al., 2011a, b; Krevor et al., 2012; Bachu, 2013). Laboratory
371 derived values available for sandstone reservoirs show S_{max} ranging between 0.31 and 0.85 and S_t
372 between 0.1 and 0.52; the Lesueur Sandstone samples tested in this study show a relatively narrow
373 range of S_{max} ($0.55 < S_{max} < 0.61$), while residual CO₂ saturation is more variable ($0.23 < S_t < 0.44$).

374 Finally, the percentage of the residually trapped CO₂ with reference to S_{max} (i.e. $R = \frac{S_t}{S_{max}}$) ranges
375 between 41.58 and 73.20 % for the Lesueur Sandstone samples (Table 7) with an average value of 61.02
376 %, in good agreement with the mean sandstone value of 61 % reported by Burnside and Naylor (2014).

377 The relationship between the maximum and residual saturations of the non-wetting fluid is often
378 estimated using the empirical trapping model developed by Land (1968) to predict the trapped gas

379 saturation as a function of the initial gas saturation. According to the model, residual saturation can be
380 calculated as:

$$S_t = \frac{S_{max}}{1 + CS_{max}} \quad \text{Eq. 6}$$

381 Where C is the trapping coefficient calculated as:

$$C = \frac{1}{S_t} - \frac{1}{S_{max}} \quad \text{Eq. 7}$$

382 It can be seen in Figure 9 that experimental observations of residual trapping of supercritical CO₂
383 reported in sandstone reservoirs are generally bounded by the Land's trapping coefficient range of 0.2
384 $< C < 5$ and that the Lesueur Sandstone samples exhibit a range of C between 0.63 and 2.55 (Table 7).

385 **5.2 Fluid-rock interaction and resulting permeability degradation**

386 The characterization analysis conducted on the samples before and after core flooding tests indicate a
387 significant alteration of some of their petrophysical properties. While the overall porosity remains
388 almost unchanged, the most evident modifications are seen in a systematic reduction of permeability
389 (measured by He permeametry) observed on the four samples analysed after flooding (Figure 10 and
390 Table 6) and in the NMR T₂ spectra collected on the brine saturated samples showing shorter T₂ (i.e.
391 less movable water) (Figure 8). The observed variations could be attributed to the fluid-rock interactions
392 occurred during the flooding experiments.

393 Fluid rock interactions during flooding of siliciclastic reservoirs with supercritical CO₂ and CO₂-
394 saturated brines can be observed in nature (e.g. Bowker et al., 1991; Emberly et al., 2005; Assayag et
395 al., 2009) and in laboratory experiments (e.g. Berrezueta et al., 2013; Huq et al., 2014; Pudlo et al.,
396 2015) with consequences reported on the permeability (Sayegh et al., 1990; Pudlo et al., 2015; Yasahura
397 et al., 2015) and elastic/mechanical properties of the host rock (Daley et al., 2007; Oikawa et al., 2008;
398 Zheng et al., 2015; Delle Piane and Sarout, submitted).

399 Injection of carbon dioxide into a brine saturated reservoir will result in the formation of carbonic acid
400 which, in turn, will likely react with the minerals constituting the porous frame of the rock, inducing
401 mineral dissolution and/or precipitation. Common reactions within quartz rich sandstone reservoirs
402 include the dissolution of carbonate and evaporite cements and the dissolution of alkali feldspar and
403 clay minerals (e.g. Gaus, 2010 and references therein). Mineral dissolution would result in an increase
404 in porosity which was not observed in our samples indicating that this fluid-rock interaction mechanism
405 was not dominant at the experimental conditions explored in this study.

406 Alternative mechanisms that could explain the observed decrease in permeability and shift in NMR
407 spectra are mineral precipitation and particle migration within the pore space of the rocks. Based on the
408 mineralogy of the Lesueur samples, potential reactive phases identified in all tested samples are K-
409 feldspar and kaolinite, while the only sample with quantifiable carbonate material was 206660 (see
410 Table 2). While feldspar reaction rates are rather sluggish at the experimental conditions explored in
411 this study, clay minerals and carbonates can react with carbonic acid quite rapidly, which can lead to
412 pore space geometry changes in a relatively short time (e.g. Vialle and Vanorio, 2011; Pudlo et al.,
413 2015). Clay minerals, in particular, are very susceptible to changes in the surface layer chemistry, and
414 recent experimental studies pointed out that CO₂ can be adsorbed onto kaolinite (Schaefer et al. 2014)
415 and that interactions between clay minerals and supercritical CO₂ and acidified brines can lead to
416 detachment and partial removal of inter-granular clay from the rock matrix as a consequence of CO₂
417 diffusion within the clay layer structures and related changes in the interlayer electrical forces
418 (Berrezueta et al., 2013; Wilson et al., 2014).

419 Kaolinite is the one of the clay minerals identified in the Lesueur Sandstone (Olierook et al., 2014) and
420 is detected by XRD in the samples used for core flooding (Table 2); it occurs as an authigenic phase
421 showing different habits including fine grained, pore occluding (Figure 11a) and pore bridging (Figure
422 11b) aggregates; booklets and vermicules growing on quartz grain surfaces (Figure 11c) and euhedral,
423 well crystallized and coarse grained (Figure 11d). It is evident that even within the same sample,
424 kaolinite crystals display considerable variation in terms of morphology and size and therefore specific
425 surface area, a critical parameter dictating the capacity of interactions with pore fluids.

426 Alteration of brine salinity and pH has been shown to modify the electrical charge of kaolinite and cause
427 repulsive forces leading to dispersion from its aggregate form and mobilization within the pore space,
428 i.e. fines migration (Lemon et al., 2011; Wilson et al., 2014), which in turn can negatively affect
429 permeability in sandstone as previously reported for example by Bennion et al. (1992), Kummerow and
430 Spangenberg (2011), Sell et al. (2013) and Pudlo et al. (2015)

431 The role of fines migration in the permeability reduction of the post-flood samples is further reaffirmed
432 by the fact that while permeability values of the samples were reduced after undergoing the flooding
433 procedure, the changes in their porosity values were not appreciable. This is in line with what has been
434 reported in the literature by other researchers (Morris and Shepperd, 1982; Priisholm et al., 1987;
435 Hayatdavoudi and Ghalambor, 1996; Musharova et al., 2012). In fact, existence of kaolinite particles
436 in the pore space of sample 206669 is evident from the Scanning Electron Microscopy (SEM) images
437 taken from the offcuts of this sample (Figure 11). During the flooding process, these particles could
438 dislodge and while moving towards the samples downstream could plug and/or bridge the samples pore
439 throats.

440 **6 Summary and Conclusions**

441 Four conventional USS core-flooding experiments were conducted on different core-plugs from the
442 Wonnerup Member of the Lesueur Formation. The main data generated by the experiments included
443 residual scCO₂ and brine saturations and relative permeabilities for the drainage and imbibition floods.

444 Overall, the experimental results indicate that significant quantities of CO₂ were trapped in the Lesueur
445 Sandstone samples by capillary forces, as a result of imbibition under in-situ reservoir conditions. While
446 the residual scCO₂ saturations obtained were relatively high, they are inversely proportional to the
447 samples' absolute permeabilities, as one may expect. Initial and residual saturations measured in this
448 study seem consistent with values published in the literature from sandstones reservoir samples.

449 Once flooded, the samples showed about 25%-60% reduction in permeability while the changes in their
450 porosity values were almost negligible. The results of all the auxiliary analysis performed point towards
451 fines migration to be the likely cause of the permeability reductions observed. This phenomenon can

452 have a significant and detrimental effect on CO₂ injectivity, and most likely can affect the near wellbore
453 region where fluid flow and chemical/physical alteration of the formation brine are maximised.

454

455 Given the petrological and petrophysical nature of the Lesueur Sandstone, it is believed that the results
456 presented here could be relevant for other sandstone reservoirs with similar mineralogy, being
457 considered for CO₂ geo-sequestration. A better understanding of the influence of isolated variables (e.g.
458 fluid pH or salinity) on the magnitude of permeability reduction should be the focus of future research.

459 **7 Acknowledgements**

460 The authors wish to acknowledge financial assistance provided through Australian National Low
461 Emissions Coal Research and Development (ANLEC R&D). ANLEC R&D is supported by Australian
462 Coal Association Low Emissions Technology Limited and the Australian Government through the
463 Clean Energy Initiative. This manuscript has been prepared based on the data and information generated
464 in ANLEC R&D funded project 7-1111-0199.

465 The authors would also like to acknowledge Geotech Geotechnical Services PTY LTD for their help
466 during the sample characterisation stage of this work. We also would like to acknowledge the help from
467 PRORES AS for granting us the access to their core-flood interpretation software package, Sendra.

468 **8 References**

- 469 Akbarabadi, M., Piri, M., 2013. Relative permeability hysteresis and permanent capillary trapping
470 characteristics of supercritical CO₂/brine systems: an experimental study at reservoir conditions.
471 *Advances in Water Resources*. 52, 190–206.
- 472 Archer, J. S., and S. W. Wong, 1973, Use of a reservoir simulator to interpret laboratory waterflood
473 data: SPE 3551, *SPE Journal*, v. 13, p. 343-347.
- 474 Assayag, N., J. Matter, M. Ader, D. Goldberg, and P. Agrinier., 2009. Water–rock interactions during
475 a CO₂ injection field-test: implications on host rock dissolution and alteration effects. *Chemical*
476 *Geology* 265, no. 1 : 227-235.
- 477 Bachu, S., 2012. Drainage and imbibition of CO₂/brine relative permeability curves at in situ conditions
478 for sandstone formations in western Canada. Proceedings of the 11th International Conference on
479 Greenhouse Gas Control Technologies, November 18–22, Kyoto, Japan, Elsevier, Energy
480 Procedia, v. 37 (2013), pp. 4428–4436
- 481 Baker, R.W. and Low, B.T., 2014. Gas Separation Membrane Materials: A Perspective.
482 *Macromolecules*, 47(20): 6999-7013.
- 483 Bear, J., 1988. Dynamics of Fluids in Porous Media. Dover Publications Inc., New York
- 484 Bennion, D.B. and Bachu, S., 2008. Drainage and imbibition relative permeability relationships for
485 supercritical CO₂/brine and H₂S/brine systems in intergranular sandstone, carbonate, shale, and
486 anhydrite rocks. *SPE Reservoir Evaluation and Engineering*, 11, pp. 487–496
- 487 Bennion, B. and Bachu, S., 2005. Relative permeability characteristics for supercritical CO₂ displacing
488 water in a variety of potential sequestration zones in the Western Canada sedimentary basin, SPE
489 95547, The SPE annual technical conference and exhibition. Society of Petroleum Engineers,
490 Dallas, Texas, USA.
- 491 Bennion, D.B., Thomas, F.B., Bennion, D.W. and Bietz, R.F., 1995. Mechanisms of formation damage
492 and permeability impairment associated with the drilling, completion and production of low API
493 gravity oil reservoirs. SPE 30320.

494 Bennion, D.B., Bietz, R.F., Thomas, F.B. and Cimolai, M.,1994. Reductions in the Productivity of Oil
495 and Low Permeability Gas Reservoirs Due to Aqueous Phase Trapping. *Journal of Canadian*
496 *Petroleum Technology* 33, No. 9

497 Bennion, D.B., Scott, JA. and Bennion, D.W., 1992. Detailed Laboratory Studies of Chemically and
498 Biologically Induced Formation Damage in the East Wilmington Field, paper CIM 92-44 presented
499 at the ATM of the Petroleum Society of CIM (May 7-10, 1992).

500 Berrezueta, E., L. González-Menéndez, D. Breitner, and L. Luquot., 2013. Pore System Changes during
501 Experimental CO₂ Injection into Detritic Rocks: Studies of Potential Storage Rocks from Some
502 Sedimentary Basins of Spain, *International Journal of Greenhouse Gas Control* 17. Elsevier Ltd:
503 411–22. doi:10.1016/j.ijggc.2013.05.023.

504 Bowker, Kent A., and P. J. Shuler.,1991. Carbon dioxide injection and resultant alteration of the Weber
505 Sandstone, Rangely Field, Colorado (1). *AAPG Bulletin* 75, No. 9 : 1489-1499.

506 Burnside, N. M., and M. Naylor., 2014. Review and implications of relative permeability of CO₂/brine
507 systems and residual trapping of CO₂. *International Journal of Greenhouse Gas Control* 23 : 1-11.

508 Busch, A., Alles, S., Gensterblum, Y., Prinz, D., Dewhurst, D.N., Raven, M.D., Stanjek, H., Krooss,
509 B.M., 2008. Carbon dioxide storage potential of shales. *International Journal of Greenhouse Gas*
510 *Control* 2, 297–308

511 Cheneviere, P., Sardin, M., de Farcy, P. and Putz, A., 1992. An equilibrium model for describing the
512 transient transport of particles in porous media. *Phys. Chem. Colloids Interfaces Oil Production*.
513 H. Toulhoat, J. Lecourtier (eds.) and editions Technip, 317-332.

514 Daley, Thomas M., Larry R. Myer, J. E. Peterson, E. L. Majer, and G. M. Hoversten. 2007. “Time-
515 Lapse Crosswell Seismic and VSP Monitoring of Injected CO₂ in a Brine Aquifer.” *Environmental*
516 *Geology* 54 (8): 1657–65. doi:10.1007/s00254-007-0943-z.

517 Delle Piane, C., Esteban, L., Timms, N.E. and Ramesh Israni, S., 2013a. Physical properties of
518 Mesozoic sedimentary rocks from the Perth Basin, Western Australia. *Australian Journal of Earth*
519 *Sciences*, 60(6-7): 735-745.

520 Delle Piane, C., Olierook, H.K.H., Timms, N.E., Saeedi, A., Esteban, L., Rezaee, R., Mikhaltsevitch,
521 V., Lebedev, Maxim. 2013b. Facies-based rock properties distribution along the Harvey 1
522 stratigraphic well. CSIRO Report Number EP133710. ANLEC Project Projects 7-1111-0199:
523 [http://www.anlecrd.com.au/literature_146941/Facies-](http://www.anlecrd.com.au/literature_146941/Facies-based_rock_properties_distribution_along_the_Harvey-1_stratigraphic_well)
524 [based rock properties distribution along the Harvey-1 stratigraphic](http://www.anlecrd.com.au/literature_146941/Facies-based_rock_properties_distribution_along_the_Harvey-1_stratigraphic_well)
525 Delle Piane, C. and Sarout J. Effects of water and supercritical CO₂ on the mechanical and elastic
526 properties of Berea sandstone. Submitted to International Journal of Greenhouse Gas Control.
527 DeVore, G.W., 1957. The surface chemistry of feldspars as an influence on their decomposition
528 products. Clays and clay minerals, vol. 6, 1, 26-41.
529 Dillinger, A. and Esteban, L., 2014. Experimental evaluation of reservoir quality in Mesozoic
530 formations of the Perth Basin (Western Australia) by using a laboratory low field Nuclear Magnetic
531 Resonance. Marine and Petroleum Geology, 57(0): 455-469.
532 Doughty, C., & Pruess, K. (2004). Modeling supercritical carbon dioxide injection in heterogeneous
533 porous media. Vadose Zone Journal, 3(3), 837-847.
534 Dullien, F.A.L.: Porous Media: Fluid Transport and Pore Structure. Academic Press Inc., New York
535 (1992)
536 Dunn, K.J., Bergman, D.J. and LaTorraca, G.A., 2002. Nuclear magnetic resonance: Petrophysical and
537 logging applications. Elsevier.
538 Emberley, S., I. Hutcheon, M. Shevalier, K. Durocher, B. Mayer, W. D. Gunter, and E. H. Perkins.
539 Monitoring of fluid-rock interaction and CO₂ storage through produced fluid sampling at the
540 Weyburn CO₂ injection enhanced oil recovery site, Saskatchewan, Canada. Applied Geochemistry
541 20, no. 6 (2005): 1131-1157.
542 Gaus, Irina. Role and impact of CO₂-rock interactions during CO₂ storage in sedimentary rocks.
543 *International journal of greenhouse gas control* 4, no. 1 (2010): 73-89.
544 Garrels, R.M. and Howard, P., 1959. Reactions of feldspar and mica with water at low temperature and
545 pressure. *Geochem. Cosmochim. Acta*, 50, 1847-1860.

546 Grigg, R.B. and Svec, R.K., 2006. CO₂ transport mechanisms in CO₂/brine core flooding, SPE 103228,
547 SPE Annual Technical Conference and Exhibition. Society of Petroleum Engineers, San Antonio,
548 Texas, USA.

549 Hayatdavoudi, A. and Ghalambor, A., 1996. Controlling Formation Damage Caused by Kaolinite Clay
550 Minerals: Part I, SPE Formation Damage Control Symposium. Copyright 1996, Society of
551 Petroleum Engineers Inc., Lafayette, Louisiana.

552 Heaviside, J. and Black, C.J.J., 1983. Fundamentals of relative permeability: experimental and
553 theoretical considerations, SPE 12173, SPE Annual Technical Conference and Exhibition. Society
554 of Petroleum Engineers of AIME, San Francisco, California.

555 Huq, Farhana, Stefan B. Haderlein, Christian Schröder, Michael AW Marks, and Peter Grathwohl.
556 Effect of injected CO₂ on geochemical alteration of the Altmark gas reservoir in Germany.
557 Environmental Earth Sciences 72, no. 9 (2014): 3655-3662.

558 IPCC: IPCC Special Report on Carbon dioxide Capture and Storage—Summary for Policymakers,
559 Report, Intergovernmental Panel on Climate Change, Montreal, Canada, 25 pp (2005).

560 Izgec, O., Demiral, B., Bertin, H. and Akin, S., 2008. CO₂ injection into saline carbonate aquifer
561 formations I: laboratory investigation Transport in porous media, 72(1): 1-24.

562 Jorand, R., Fehr, A., Koch, A. and Clauser, C., 2011. Study of the variation of thermal conductivity
563 with water saturation using nuclear magnetic resonance. Journal of Geophysical Research: Solid
564 Earth, 116(B8): B08208.

565 Khan, L. and Hasan, M., 2007. Enhancement of hydrophylic characteristics of non-wetting porous
566 substrates by kaolinite treatment. SAE technical paper, 2007-01-3178, doi: 10.4271/2007-01-3178.

567 Kleinberg, R.L. et al., 2003a. Deep sea NMR: Methane hydrate growth habit in porous media and its
568 relationship to hydraulic permeability, deposit accumulation, and submarine slope stability.
569 Journal of Geophysical Research: Solid Earth, 108(B10): 2508.

570 Kleinberg, R.L. et al., 2003b. Seafloor nuclear magnetic resonance assay of methane hydrate in
571 sediment and rock. Journal of Geophysical Research: Solid Earth, 108(B3): 2137.

572 Kopp, A., H. Class, and R. Helmig (2009), Investigations on CO₂ storage capacity in saline aquifers
573 Part 1. Dimensional analysis of flow processes and reservoir characteristics, *Int. J. Greenhouse*
574 *Gas Control*, 3, 263–276

575 Krevor, S.C.M., Pini, R., Zuo, L., Benson, S.M. Relative permeability and trapping of CO₂ and water
576 in sandstone rocks at reservoir conditions. *Water Resource Research*, 48 (2012), p. W02532
577 <http://dx.doi.org/10.1029/2011WR010859>

578 Kummerow, Juliane, and Erik Spangenberg. Experimental evaluation of the impact of the interactions
579 of CO₂-SO₂, brine, and reservoir rock on petrophysical properties: A case study from the Ketzin
580 test site, Germany. *Geochemistry, Geophysics, Geosystems* 12, no. 5 (2011).

581 Labus, K., 2010. Modeling CO₂ sequestration mechanisms, and capacity of carboniferous aquifer rocks
582 of the Upper Silesian Coal Basin (Poland, Czech Republic). *Water-rock interaction - Birkle &*
583 *Torres-Alvarado (eds.)*, Taylor & Francis Group, London, ISBN: 978-0-415-60426-0, 871-875.

584 Land CS (1968) Calculation of imbibition relative permeability for two and three-phase flow from rock
585 properties. *Society of Petroleum Engineers Journal*, 8, 149–56.

586 Lemon, Phillip Edward, Abbas Zeinijahromi, Pavel G. Bedrikovetsky, and Ibrahim Shahin. Effects of
587 injected water chemistry on waterflood sweep efficiency via induced fines migration. In *SPE*
588 *International Symposium on Oilfield Chemistry*. Society of Petroleum Engineers, 2011.

589 Li, X., Akbarabadi, M., Karpyn, Z.T., Piri, M., Bazilevskaya, E., 2015. Experimental investigation of
590 carbon dioxide trapping due to capillary retention in saline aquifers. *Geofluids*,
591 <http://dx.doi.org/10.1111/gfl.12127>.

592 Liu, H., D'Eurydice, M.N.m Obruchkiv, S. and Galvosas, P., 2014. Pore length scales and pore surface
593 relaxivity of sandstone determined by internal magnetic fields modulation at 2 MHz NMR.
594 *Diffusion fundamentals*, 22, 7, 1-5.

595 Lu, J., Kordi, M., Hovorka, S.D., Meckel, T.A., Christopher, C.A., 2012. Reservoir characterisation and
596 complications for trapping mechanisms at Cranfield CO₂ injection site. *Int. J. Greenh. Gas Control*.

597 Mackay, E., Pickup, G., Olden, P. Rock mechanics, geochemistry and aquifer fluid flow. CASSEM
598 Conference, 4th October 2010, Edinburgh (2010)

599 Manrique, E.J., Muci, V.E., Gurfinkel, M.E.: EOR field experiences in carbonate reservoirs in the
600 United States. SPE Reserv. Eval. Eng. 10, 667–686 (2007)

601 Millar, AS and Reeve, J (compilers) 2014, GSWA Harvey 1 well completion and preliminary
602 interpretation report, southern Perth Basin:Geological Survey of Western Australia, Record
603 2014/12, 17p.

604 Morris, K.A. and Shepperd, C.M., 1982. The role of clay minerals in influencing porosity and
605 permeability characteristics in the bridport sands of wytch farm, dorset. Clay Minerals, 17: 41-54.

606 Morriss, C.E., MacInnis, J., Freedman, R. and Smaardyk, J., 1993. Field Test Of An Experimental
607 Pulsed Nuclear Magnetism Tool, SPWLA 34th Annual Logging Symposium. Society of
608 Petrophysicists and Well-Log Analysts, Calgary, Alberta

609 Müller, N. (2011). Supercritical CO₂-brine relative permeability experiments in reservoir rocks—
610 Literature review and recommendations. Transport in porous media, 87(2), 367-383.

611 Musharova, D., Mohamed, I.M. and Nasr-El-Din, H.A., 2012. Detrimental Effect of Temperature on
612 Fines Migration in Sandstone Formations, SPE International Symposium and Exhibition on
613 Formation Damage Control. Society of Petroleum Engineers, Lafayette, Louisiana, USA.

614 Nicot, B., Gautier, S., Fleury, M. and Durucan, S., 2006. Pore Structure Analysis of Coals Using Low
615 Field NMR Measurements and Thermogravimetric Analysis, SCA2006-27, The International
616 Symposium of the Society of Core Analysts, Trondheim, Norway

617 Oikawa, Y., T. Takehara, and T. Tosha. Effect of CO₂ injection on mechanical properties of Berea
618 Sandstone. In The 42nd US Rock Mechanics Symposium (USRMS). American Rock Mechanics
619 Association, 2008.

620 Olierook, H.K.H. et al., 2014. Facies-based rock properties characterization for CO₂ sequestration:
621 GSWA Harvey 1 well, Western Australia. Marine and Petroleum Geology, 50: 83-102.

622 Marschall, D., Gardner, J.S., Mardon, D. and Coates, G.R., 1995. Method for correlating NMR
623 relaxometry and mercury injection data. SCA, Conference paper 9511, 1-12.

624 Pentland, C.H., El-Maghraby, R., Iglauer, S., Blunt, M.J., 2011. Measurements of the capillary trapping
625 of super-critical carbon dioxide in Berea sandstone. *Geophys. Res. Lett.* 38, L06401.

626 Pentland, C.H., El-Maghraby, R. Georgiadis, A., Iglauer, S. Blunt, M.J. Immiscible displacements and
627 capillary trapping in CO₂ storage. *Energy Procedia*, 4 (2011), pp. 4969–4976

628 Perrin, J.-C. and Benson, S.M., 2010. An experimental study on the influence of sub-core scale
629 heterogeneities on CO₂ distribution in reservoir rocks. *Transport in porous media*, 82(1): 93-109.

630 Priisholm, S., Nielsen, B.L. and Haslund, O., 1987. Fines migration, blocking, and clay swelling of
631 potential geothermal sandstone reservoirs, Denmark. *SPE 15199, SPE Formation Evaluation*, 2(2):
632 168-178.

633 Pudlo, Dieter, Steven Henkel, Viktor Reitenbach, Daniel Albrecht, Frieder Enzmann, Katja Heister,
634 Geertje Pronk, Leonhard Ganzer, and Reinhard Gaupp. The chemical dissolution and physical
635 migration of minerals induced during CO₂ laboratory experiments: their relevance for reservoir
636 quality. *Environmental Earth Sciences* 73, no. 11 (2015): 7029-7042.

637 Rapoport, L.A. and Leas, W.J., 1953. Properties of linear waterfloods. *SPE 213-G, Petroleum*
638 *Transactions, AIME*, 198: 139-148.

639 Ruprecht, C., Pini, R., Falta, R., Benson, S., Murdoch, L., 2014. Hysteretic trapping and relative
640 permeability of CO₂ in sandstone at reservoir conditions. *Int. J. Greenh. Gas Control* 27, 15–27.

641 Saeedi, A., 2012. *Experimental Study of Multiphase Flow in Porous Media during CO₂ Geo-*
642 *Sequestration Processes*. Sprinegr Thesis. Springer Publishing, Heidelberg, Germany.

643 Saeedi, A., Rezaee, R., Evans, B. and Clennell, B., 2011. Multiphase flow behaviour during CO₂ geo-
644 sequestration: Emphasis on the effect of cyclic CO₂-brine flooding. *Journal of Petroleum Science*
645 *and Engineering*, 79(3-4): 65-85.

646 Schaef, H T, V.-a. Glezakou, a T Owen, S Ramprasad, P F Martin, and B. P. McGrail. 2014. Surface
647 Condensation of CO₂ onto Kaolinite. *Environmental Science & Technology Letters* 1 (2): 142–45.
648 doi:10.1021/ez400169b

649 Sell, Kathleen, Frieder Enzmann, Michael Kersten, and Erik Spangenberg. Microtomographic
650 quantification of hydraulic clay mineral displacement effects during a CO₂ Sequestration
651 experiment with saline aquifer sandstone. *Environmental science & technology* 47, no. 1 (2012):
652 198-204.

653 Shell. UK Carbon Capture and Storage Demonstration Competition. UKCCS-KT-S7.19-Shell-002,
654 SCAL Report ScottishPower CCS Consortium (2011), p. 59.

655 Shi, J-Q., Xue, Z., Durucan, S., 2011a. Supercritical CO₂ core flooding and imbibition in Berea
656 sandstone—CT imaging and numerical simulation *Energy Procedia*, 4 (2011), pp. 5001–5008

657 Shi, J-Q., Xue, Z., Durucan, S., 2011b. Supercritical CO₂ core flooding and imbibitions in Tako
658 sandstone – influence of sub-core scale heterogeneity. *Int. J. Greenh. Gas Control* 5, 75–87

659 Sigmund, P.M. and McCaffery, F.G., 1979. An improved unsteady-state procedure for determining the
660 relative-permeability characteristics of heterogeneous porous media. SPE 6720, *SPE Journal*,
661 19(1): 15-28.

662 Sing K, Everett D, Haul R, Moscou L, Pierotti R, Rouquérol J, Siemieniewska T (1985). IUPAC
663 Commission on colloid and surface chemistry including catalysis. Reporting physisorption data
664 for gas/solid systems with special reference to the determination of surface area and porosity
665 (Recommendations 1984). *Pure Appl Chem* 57:603–619

666 Sorland, G.H., Djurhuus, K., Wideroe, H.C., Lien, J.R. and Skauge, A., 2007. Absolute pore size
667 distributions from NMR. *Diffusion fundamentals*, 5, 4.1-4.15.

668 Suekane, T., Nobuso, T., Hirai, S., Kiyota, M., 2008. Geological storage of carbon dioxide by residual
669 gas and solubility trapping. *Int. J. Greenh. Gas Control* 2, 58–64

670 Timms N.E., Olierook, H.K.H., Wilson, M.E.J., Delle Piane, C., Hamilton, P.J., Cope, P., Stutenbecker,
671 L. 2015. Sedimentary facies analysis, mineralogy and diagenesis of the Mesozoic aquifers of the
672 central Perth Basin. *Marine and Petroleum Geology*, 60, 54-78.

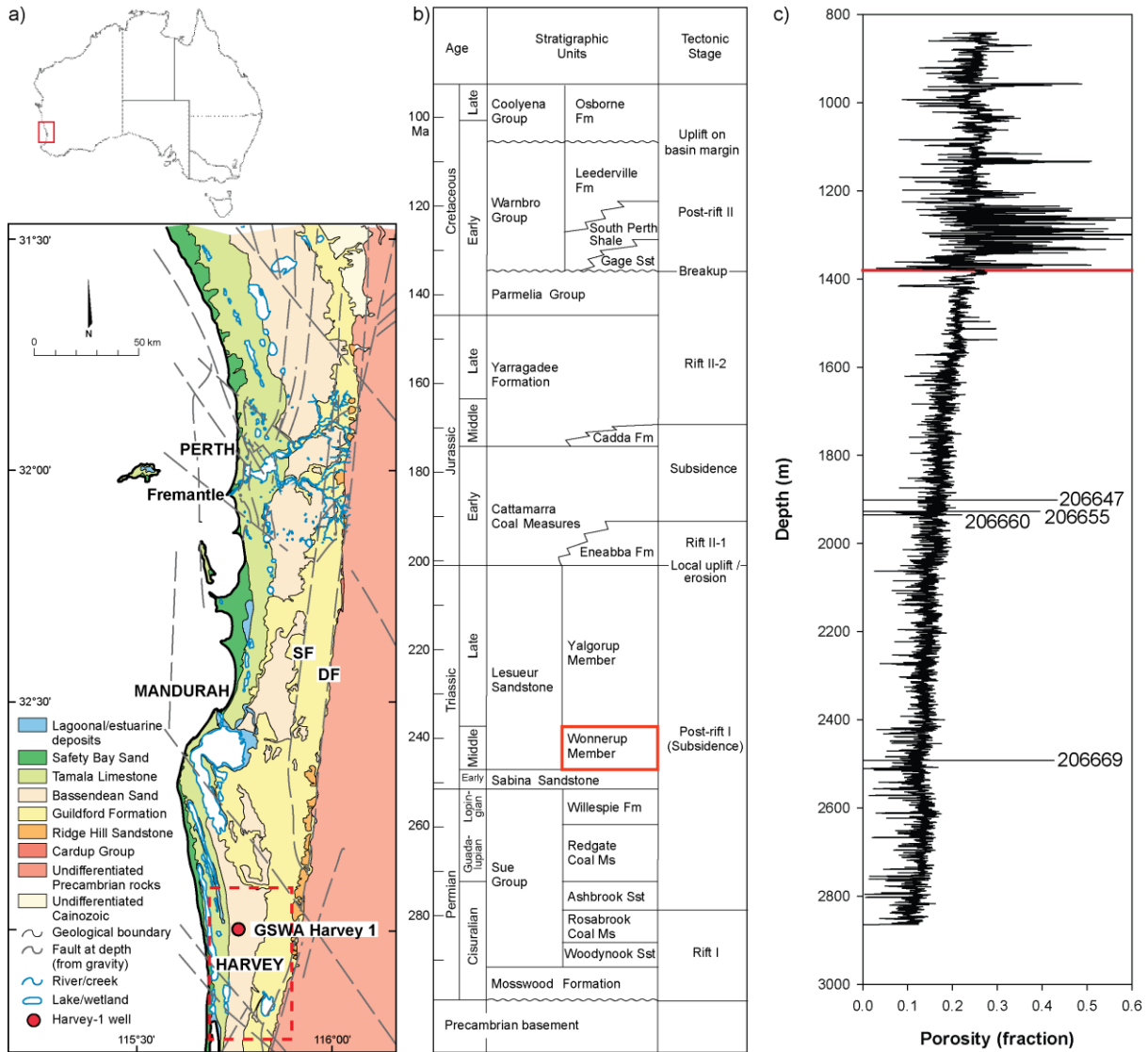
673 Vialle, Stéphanie, and Tiziana Vanorio. Laboratory measurements of elastic properties of carbonate
674 rocks during injection of reactive CO₂-saturated water. *Geophysical Research Letters* 38, no. 1
675 (2011).

676 Wilson, M. J., L. Wilson, and I. Patey. The influence of individual clay minerals on formation damage
677 of reservoir sandstones: a critical review with some new insights. *Clay Minerals* 49, no. 2 (2014):
678 147-164.

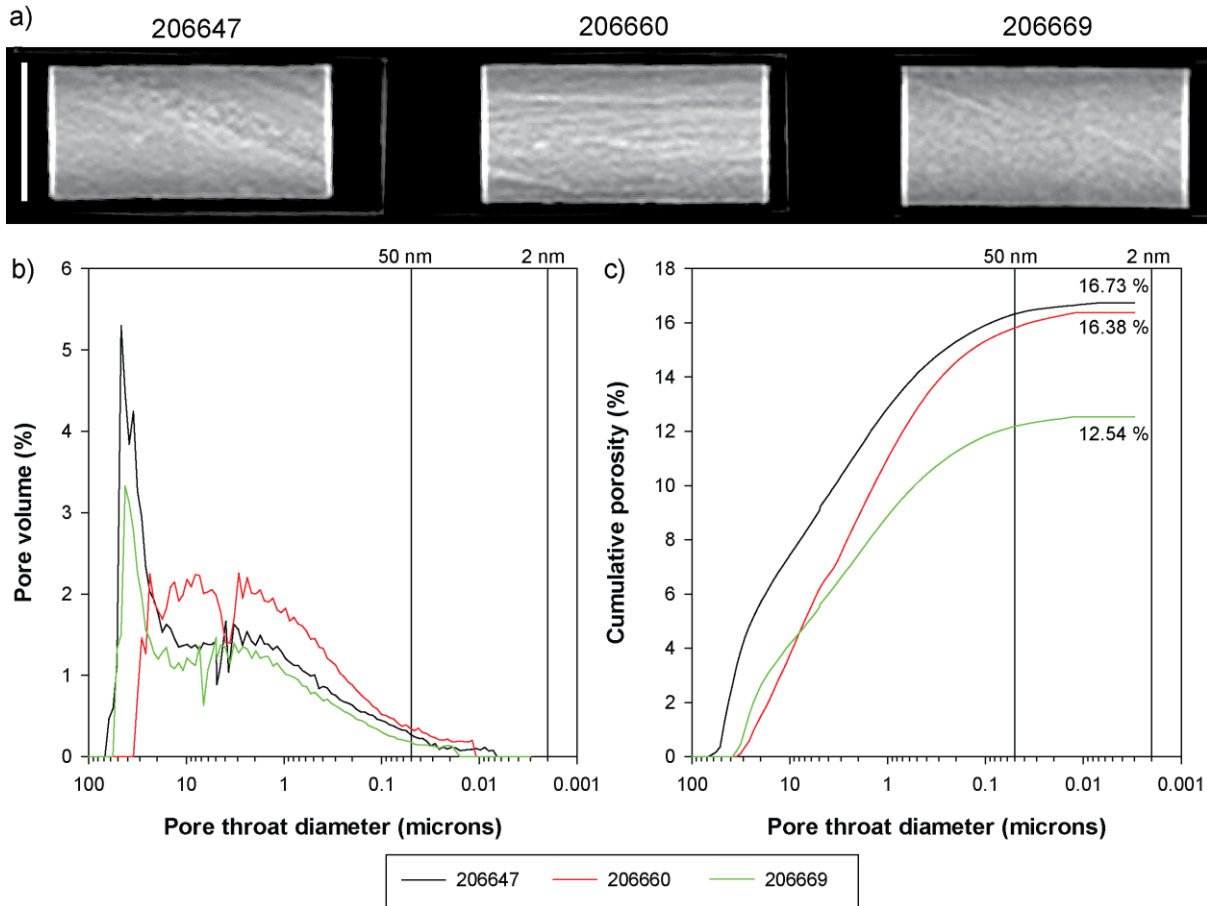
679 Yasuhara, Hideaki, Naoki Kinoshita, Hiroaki Ohfuji, Manabu Takahashi, Kazumasa Ito, and Kiyoshi
680 Kishida. Long-term observation of permeability in sedimentary rocks under high-temperature and
681 stress conditions and its interpretation mediated by microstructural investigations. *Water Resources*
682 *Research* 51, no. 7 (2015): 5425-5449.

683 Zheng, Hong, Xia-Ting Feng, and Peng-Zhi Pan. Experimental investigation of sandstone properties
684 under CO₂-NaCl solution-rock interactions. *International Journal of Greenhouse Gas Control* 37
685 (2015): 451-470.

686 Zuo, L., Benson, S.M., 2014. Process-dependent residual trapping of CO₂ in sandstone. *Geophys. Res.*
687 *Lett.* 41, 2820–2826.

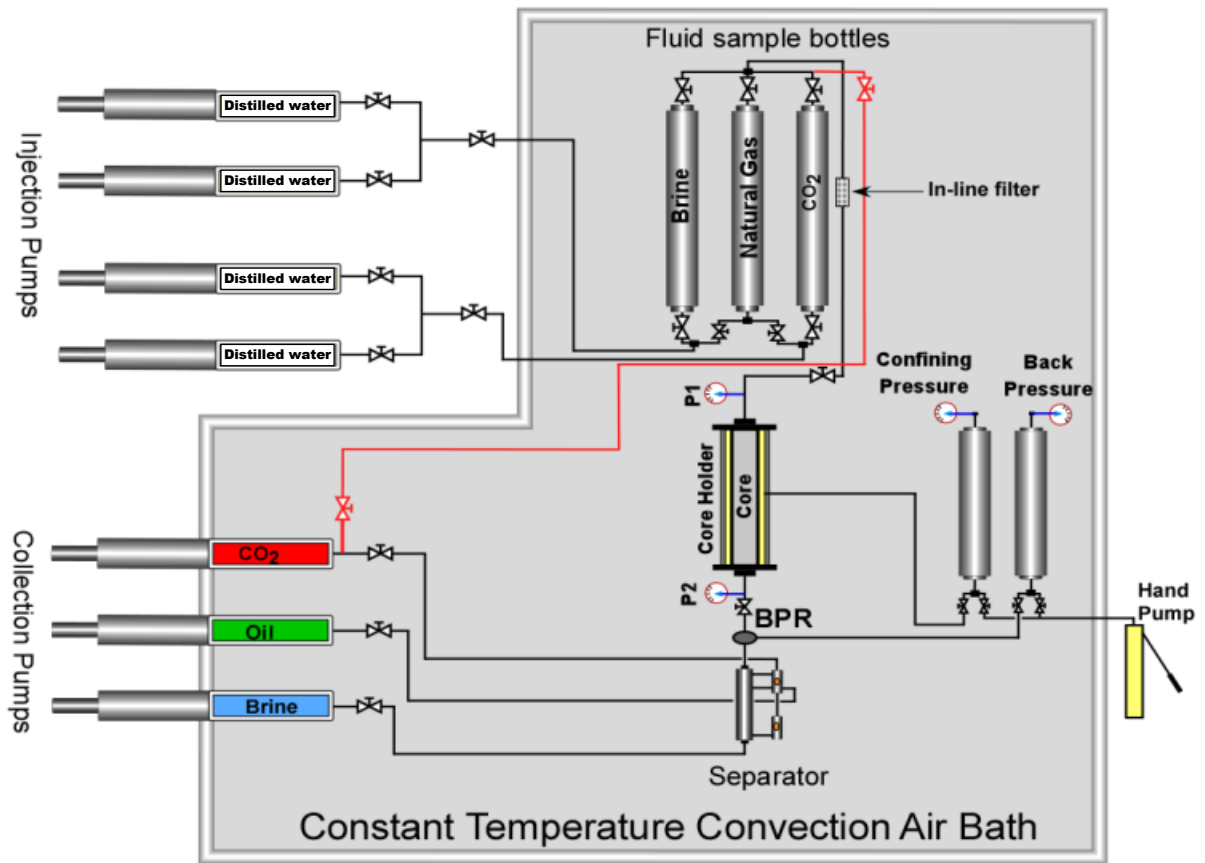


688
 689 **Figure 1 (a) Location of the Harvey-1 well and surface geology of the Perth Basin, the red dashed box indicates the**
 690 **approximate location of the proposed South-West Hub; (b) Stratigraphy of the Central and Southern Perth Basin, the**
 691 **studied section is highlighted in red (modified after Olierook et al., 2014); (c) wireline log of porosity along the Harvey**
 692 **1 well: black horizontal lines indicate the depth of each sample used in this study; red horizontal lines marks the**
 693 **transition between the Wonerup and the Yalgorup Members of the triassic Lesueur Sandstone**



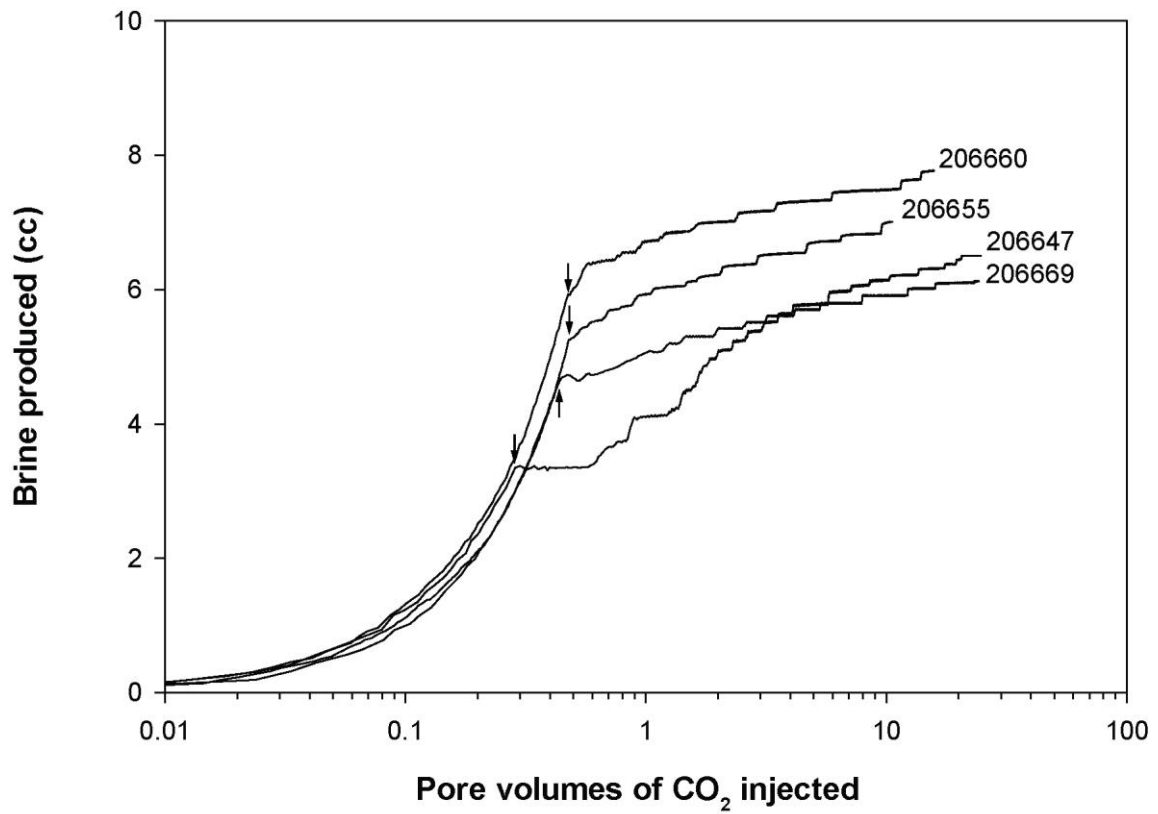
694
695
696
697
698

Figure 2 (a) X-ray CT images of three samples prior to core-flooding tests with their corresponding bulk density. (b) pore size distribution as measured by mercury injection porosimetry on offcuts of the three samples; vertical lines mark the boundaries between micropores (< 2 nm), mesopores (2-50 nm); and macropores (> 50 nm); (c) cumulative porosity as a function of pore throat size as measured by mercury injection.



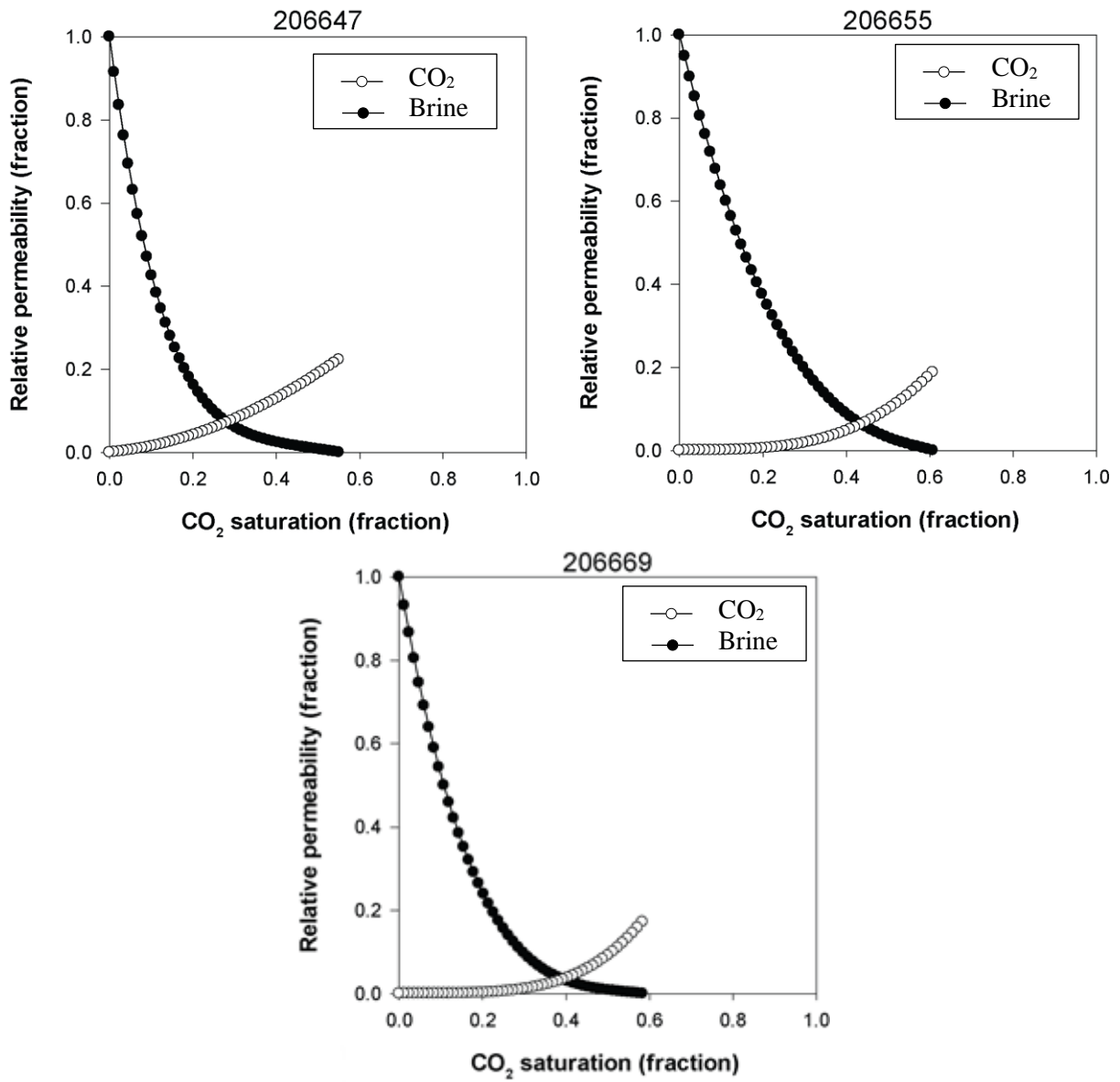
699
 700
 701

Figure 3. The schematic diagram of the experimental apparatus used to run the core-flooding experiments.



702
 703
 704
 705

Figure 4. Brine production profiles for the primary drainage conducted on three out of the four samples; breakthrough of CO₂ is indicated by the black arrow and corresponds to the change in slope of the production curves.



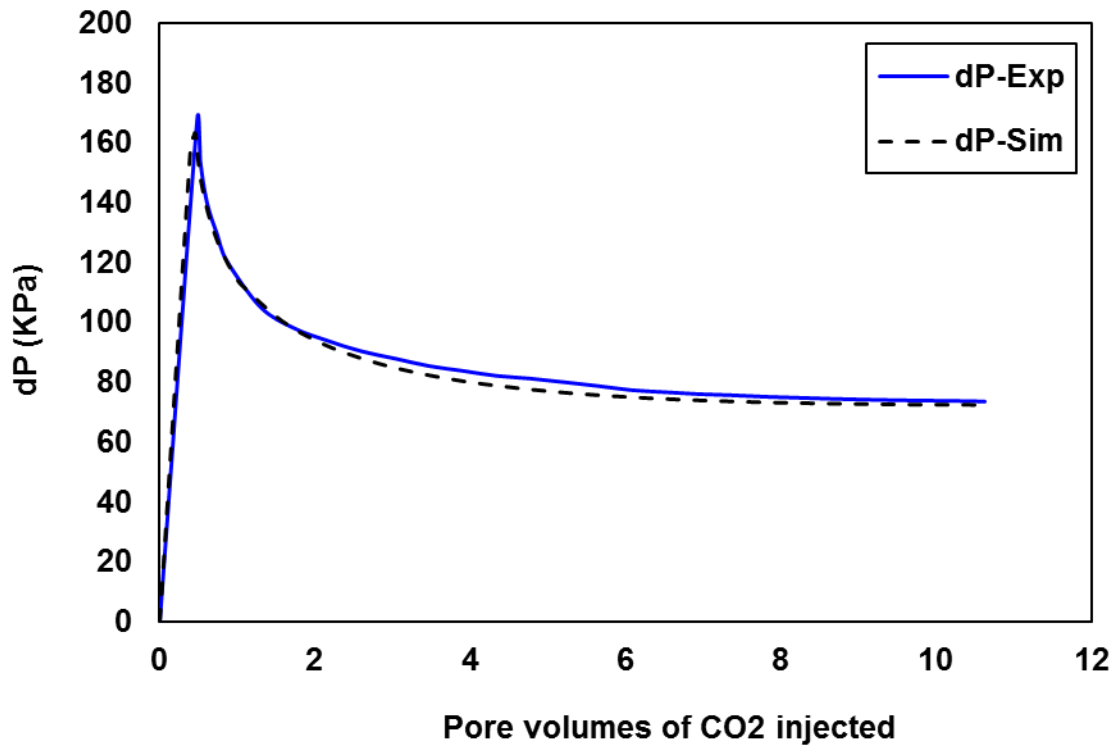
706

707

708

Figure 5. Relative permeability curves for the primary drainage conducted on the four samples.

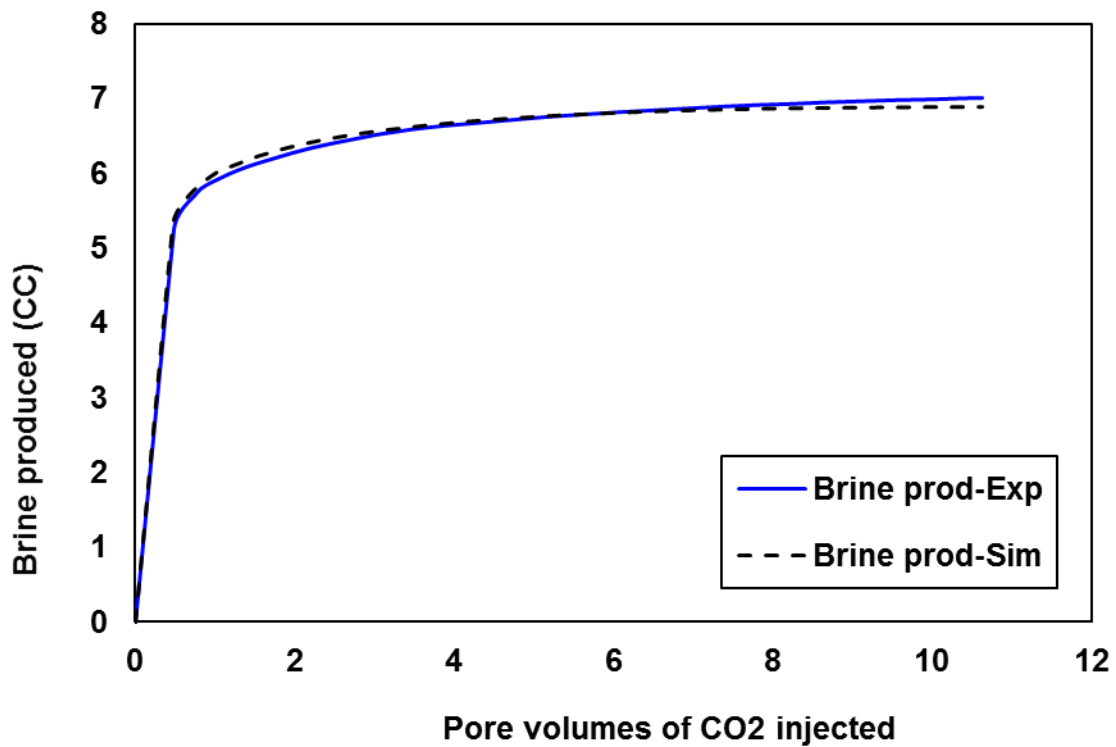
709



710

711 Figure 6. Comparison between the differential pressure profiles for Sample 206655: blue: experimental data (used in
 712 Sendra software), black: numerical simulation results (Eclipse software (Schlumberger)).

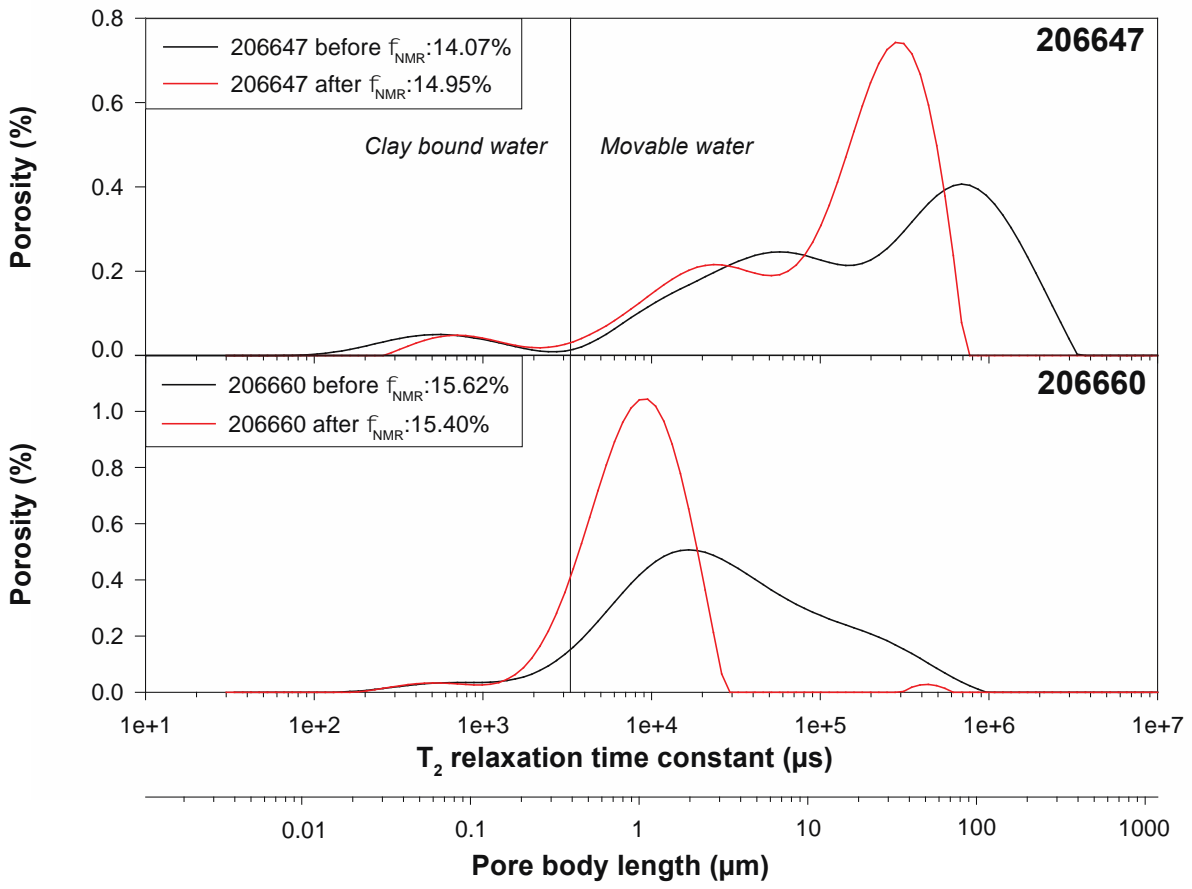
713



714

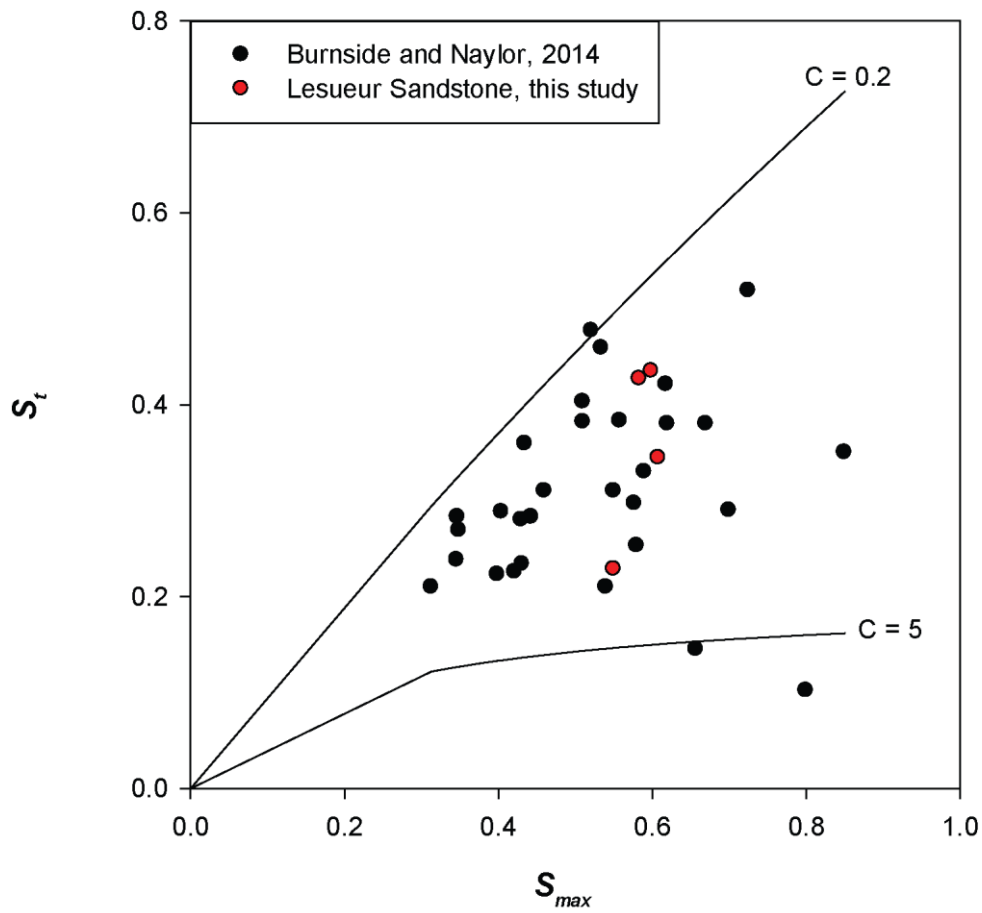
715 Figure 7. Comparison between the brine production profiles for Sample 206655: blue: experimental data (used in
 716 Sendra software), black: numerical simulation results (Eclipse software (Schlumberger)).

717



719
 720
 721
 722
 723

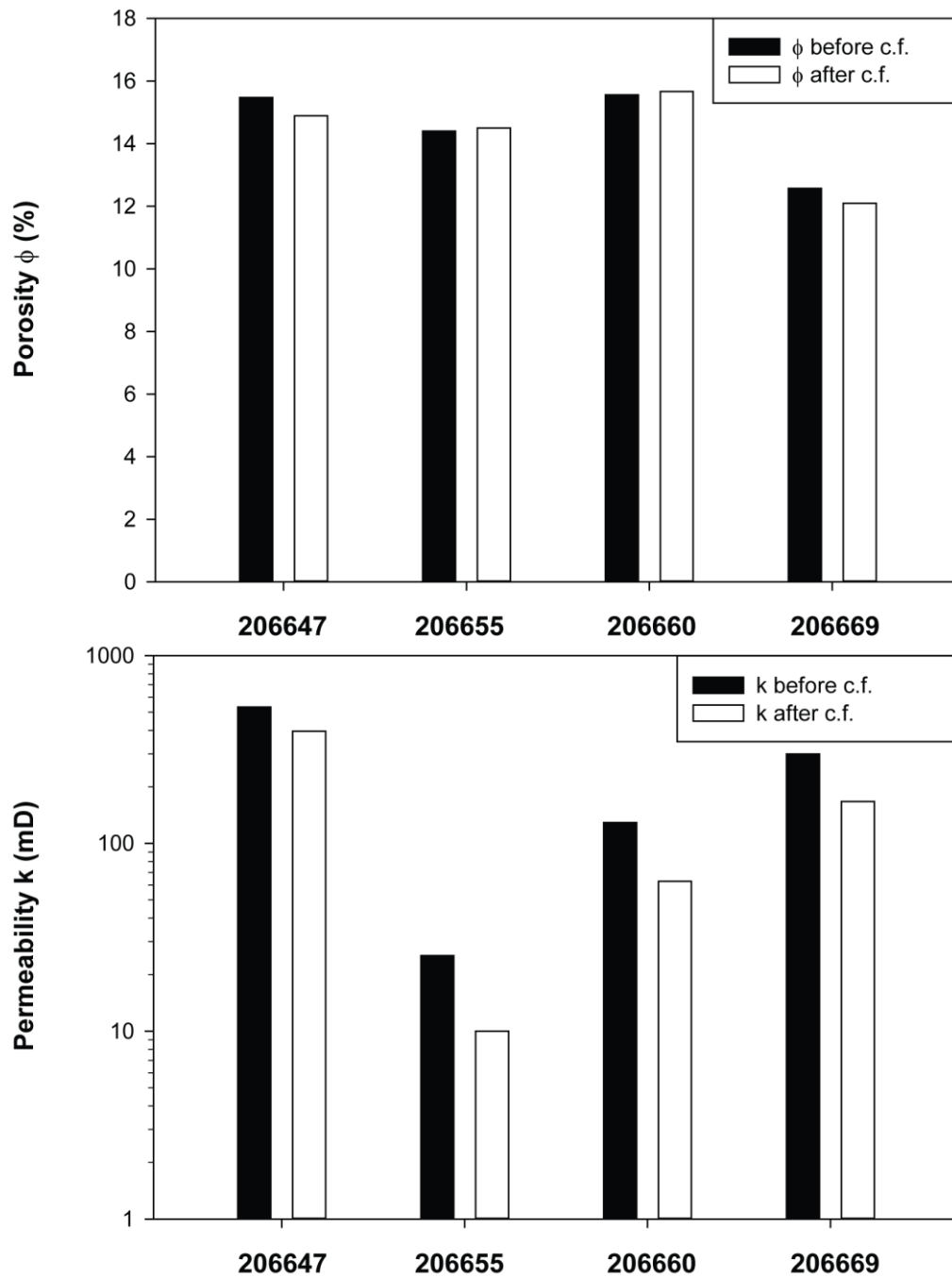
Figure 8. NMR T2 relaxation time distribution for two samples before and after core-flooding experiments. The total porosity is almost not affected by the flooding tests but the relaxation time curve for the same sample is significantly different..



724

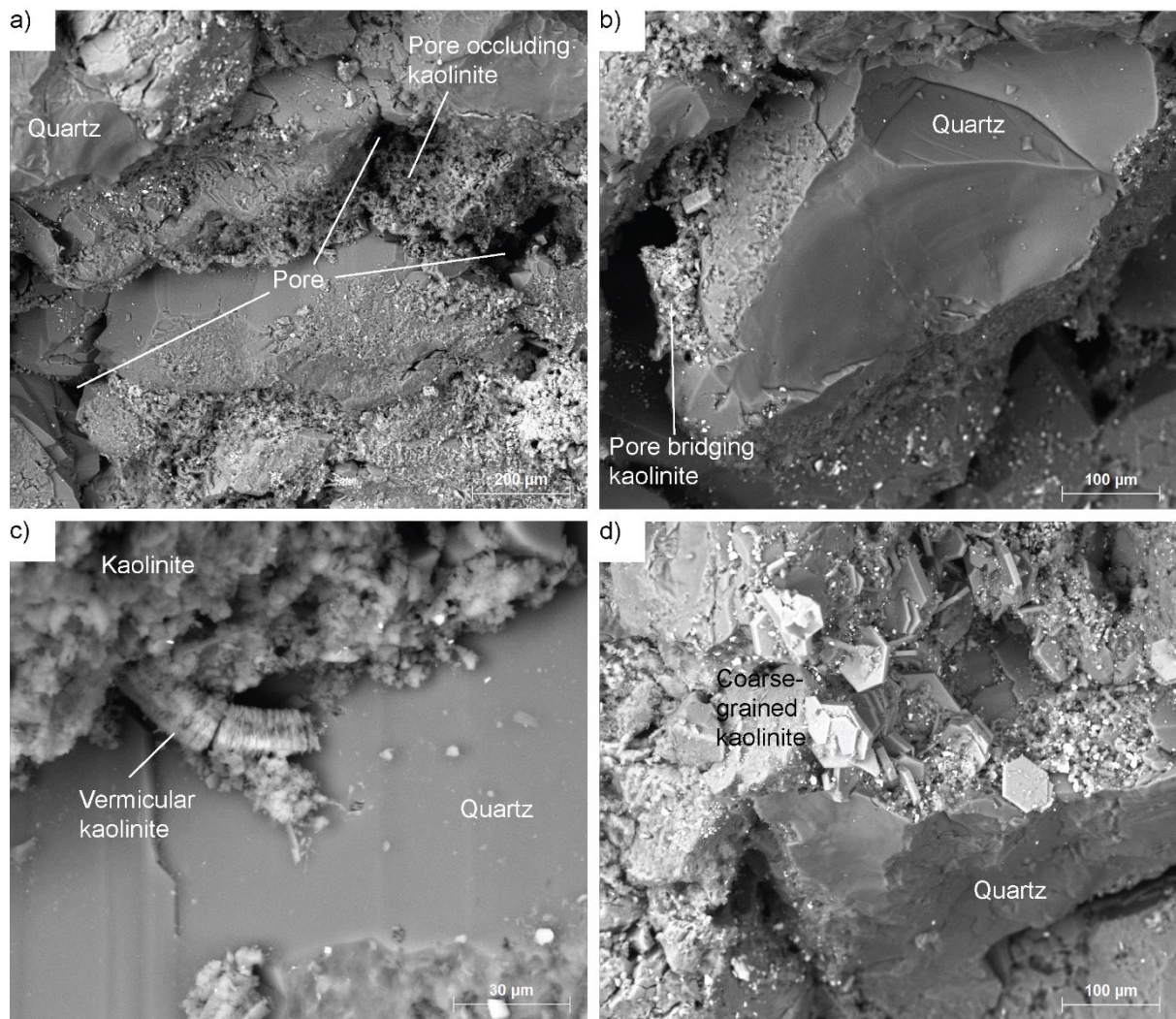
725 **Figure 9. Scatter plot of residual (S_r) versus initial CO₂ saturation (S_{max}) obtained during core flooding experiments.**
 726 **Black dots represent sandstone related experimental data available in the open literature synthesised in the review**
 727 **from Burnside and Naylor, 2014. Continuous lines represent Land's model curves with trapping coefficient (C) of 0.2**
 728 **and 5.**

729



730
 731 **Figure 10. Porosity (Top) and gas permeability (Bottom) measured using the helium on four core plugs before and after**
 732 **core flooding experiments. Note that while the variation in porosity is minimal, there is a significant decrease in**
 733 **permeability of all four sample.**

734



735

736 **Figure 11. SEM images of sample 206669 showing the occurrence of diagenetic, kaolinite (Kaol in the figure) partially**
 737 **occluding the pores between detrital quartz grains (a); bridging pores between detrital grains (b). (c) vermicular**
 738 **diagenetic kaolinite growing on a quartz crystal surface. (d) well crystallized coarse-grained kaolinite.**

739

740 **Table 1. Reservoir P-T conditions during the experiment on the four core-plugs.**

| Reservoir parameter | Sample ID | | | |
|-------------------------------------|-----------|---------|---------|---------|
| | 206647 | 206647 | 206660 | 206669 |
| Depth, m | 1,901.6 | 1,927.0 | 1,935.5 | 2,491.6 |
| Pore pressure (MPa) | 19.05 | 19.06 | 19.39 | 24.95 |
| Overburden pressure (MPa) | 43.02 | 43.59 | 43.78 | 56.36 |
| Reservoir temperature (°C) | 60.7 | 61.0 | 61.2 | 69.2 |
| Formation water salinity (ppm NaCl) | 30,000 | 30,000 | 30,000 | 30,000 |

741

742 **Table 2. Characteristics of the core-plugs used for the experiments and XRD derived mineralogy (in weight %). No**
 743 **XRD data is available for core-plug 206655. He ϕ = helium porosity; He k = helium permeability; Qz = quartz; K-feld**
 744 **= K-feldspar; Kaol = kaolinite; Ank = ankerite.**

| Sample ID | Depth (m) | He ϕ (%) | He k (mD) | Hg ϕ | Brine k (mD) | Qz | K-feld | Kaol | Ank |
|-----------|--------------|------------------|--------------|-----------|-----------------|-----|--------|------|-----|
| 206647 | 1,901.6 | 15.47 | 532 | 16.73 | 48.0 | 86 | 10 | 4 | - |
| 206655 | 1,927.0 | 14.33 | 25 | | 4.65 | N/A | N/A | N/A | N/A |
| 206660 | 1,935.5 | 15.56 | 129 | 16.38 | 16.5 | 77 | 12 | 7 | 4 |
| 206669 | 2,491.6 | 12.57 | 299 | 12.54 | 238 | 90 | 8 | 2 | - |

745 **Table 3. End-point residual saturations and relative permeabilities.**

| Sample ID | End-point Residual Saturation of the Displaced Fluid, % | | | End-point Relative permeabilities for the Displacing Fluid, fraction | | |
|-----------|---|--------------------|--------------------|--|--------------------|--------------------|
| | Primary Drainage | Primary Imbibition | Secondary Drainage | Primary Drainage | Primary Imbibition | Secondary Drainage |
| 206647 | 45.00 | 22.87 | 44.22 | 0.223 | 0.353 | 0.230 |
| 206655 | 39.2 | 43.5 | ----- | 0.188 | 0.25 | ----- |
| 206660 | 40.12 | 42.71 | ----- | 0.206 | 0.125 | ----- |
| 206669 | 41.65 | 34.47 | 41.84 | 0.172 | 0.096 | 0.15 |

747 **Table 4. Best-fit relative permeability parameters for core-floods fit to the Sigmund and McCaffery (1979) model**

| Sample ID | N_w | N_g | A | B |
|-----------|--------|--------|--------|--------|
| 206647 | 4.6335 | 1.9109 | 0.0895 | 0.2336 |
| 206655 | 2.8124 | 3.3497 | 0.1581 | 0.0051 |
| 206669 | 3.5880 | 4.1398 | 0.0538 | 0.0018 |

750 **Table 5. Rock and fluid properties used to construct the numerical model for Sample 206655 in Eclipse.**

| Fluid properties | | |
|-------------------|----------------------------|-------------------------|
| Fluid | Density, kg/m ³ | Viscosity, Pa.s |
| scCO ₂ | 705 | 0.58 x 10 ⁻⁴ |
| Brine | 1010 | 4.8 x 10 ⁻⁴ |
| Rock properties | | |
| Permeability, mD | Porosity, % | |
| 4.65 | 14.3 | |

754 **Table 6. Porosity and permeability measurements on pre- and post-core flooding experiments from the four core-**
 755 **plugs using helium and NMR methods. He ϕ = Helium porosity; NMR ϕ = NMR porosity; He k = Helium**
 756 **permeability; b.f. = before flooding; a.f. = after flooding.**

| Sample ID | He ϕ | He ϕ | NMR ϕ | NMR ϕ | He k | He k |
|---------------|-----------|-----------|------------|------------|------|-------|
| | b.f. | a. f. | b. f. | a. f. | b.f. | a. f. |
| | (%) | (%) | % | (%) | (mD) | (mD) |
| 206647 | 15.47 | 15.87 | 14.07 | 14.95 | 532 | 464 |
| 206655 | 14.33 | 14.4 | - | - | 25 | 10 |
| 206660 | 15.56 | 16.4 | 15.62 | 15.4 | 129 | 72 |
| 206669 | 12.57 | 12.75 | 11.95 | - | 299 | 188 |

757

758

759

760 **Table 7. Initial CO₂ saturation (S_{max}), residual CO₂ saturation (S_t), percentage of residually trapped CO₂ (R) and**
 761 **Land's trapping coefficient C for the Lesueur Sandstone sample tested in this study**

| Sample ID | S_{max} | S_t | R (S_t/S_{max}) | C |
|---------------|-----------|-------|---------------------|------|
| | (-) | (-) | % | (%) |
| 206647 | 0.55 | 0.23 | 41.58 | 2.55 |
| 206655 | 0.60 | 0.44 | 72.62 | 0.63 |
| 206660 | 0.58 | 0.43 | 73.20 | 0.63 |
| 206669 | 0.61 | 0.34 | 56.69 | 1.26 |

762